

This Work has been submitted to Journal of Atmospheric and Oceanic Technology.
Copyright in this Work may be transferred without further notice.

1 This manuscript is a revised version that has been submitted for publication in JOURNAL OF
2 ATMOSPHERIC AND OCEANIC TECHNOLOGY. Please note that, despite having
3 undergone peer-review, the manuscript has yet to be formally accepted for publication.
4 Subsequent versions of this manuscript may have slightly different content. If accepted, the
5 final version of this manuscript will be available via the 'Peer-reviewed Publication DOI'
6 link on the right-hand side of this webpage. Please feel free to contact any of the authors; we
7 welcome feedback

8

9

This Work has been submitted to Journal of Atmospheric and Oceanic Technology.
Copyright in this Work may be transferred without further notice.

10 **DINEOF Interpolation of Global Ocean Color Data: Error Analysis and**
11 **Masking**

12

13 Haipeng Zhao,^{a,b} Atsushi Matsuoka,^c Manfredi Manizza,^d Amos Winter^a

14 ^a *Department of Earth and Environmental Systems, Indiana State University, Terre Haute, IN, USA.*

15 ^b *Division of Earth and Climate Sciences, Nicholas School of the Environment, Duke University, Durham, NC,*
16 *USA.*

17 ^c *Institute for the Study of Earth, Oceans, and Space, University of New Hampshire, Durham, NH, USA.*

18 ^d *Geosciences Research Division, Scripps Institution of Oceanography, University of California, San Diego, La*
19 *Jolla, CA, USA.*

20

21 *Corresponding author: Haipeng Zhao (h.zhao@duke.edu)*

22

23

ABSTRACT

24 The Data Interpolation Empirical Orthogonal Function (DINEOF) algorithm is used to
25 reconstruct datasets of geophysical and biological variables such as sea surface temperature
26 (SST) and Chlorophyll *a* (Chl *a*). In this study, we analyze the impact of both the quantity
27 and distribution of missing data on the performance of DINEOF demonstrating how DINEOF
28 plus a connectivity mask can be used for future data reconstruction tasks. We propose an
29 enhanced version of DINEOF (DINEOF+) by adding two steps: (1) Using a 75% threshold of
30 missing data for reconstructing incomplete datasets and (2) Masking interpolated points that
31 lacks sufficient space-time observations in the original dataset. We successfully apply
32 DINEOF+ to the OC-CCI global daily Chl *a* dataset and validate the results using *in situ*
33 datasets. We find that the recovery rate varies across ocean basins and years. In oligotrophic
34 waters, the daily data coverage increased by 40–50% during the period from 2003 to 2020.
35 Using DINEOF+ allows us to obtain a significantly higher temporal resolution of global Chl
36 *a* data, which will improve understanding of marine phytoplankton dynamics in response to
37 changing environments.

38

SIGNIFICANCE STATEMENT

39 We perform an error analysis on the application of DINEOF for reconstructing a global
40 Chl *a* dataset. The results of this analysis illustrate the impact of missing data—both in terms
41 of quantity and distribution—on the performance of DINEOF. We propose using DINEOF+,
42 an enhanced version of DINEOF that adds an editing step to mask out interpolated points
43 based on the number of surrounding observations in the original input. The performance of
44 DINEOF+ was validated using both simulated and *in situ* datasets. The results indicate that
45 employing this masking technique effectively reduces biased estimates of missing data.
46 DINEOF+ can be applied to other biogeochemical variables. However, caution is advised
47 when dealing with observations characterized by high variance.

48 **1. Introduction**

49 Over the last two decades, observational and modeling studies have shown that ocean
50 warming is driving changes in phytoplankton production and distribution (Behrenfeld et al.
51 2006; Benedetti et al. 2021; Gobler et al. 2017). Increased frequency of extreme events and
52 variations in nutrient supply as a result of both changing circulation and stratification are
53 likely to reorganize the dynamics of phytoplankton communities, leading to far-reaching

This Work has been submitted to Journal of Atmospheric and Oceanic Technology.
Copyright in this Work may be transferred without further notice.

54 impacts on local ecosystems and human society (Huntington et al. 2020; Smith et al. 2021).
55 Nevertheless, the task of establishing concrete connections between environmental variables
56 and phytoplankton response has been formidable (Behrenfeld and Boss 2014).

57 The use of ocean color data, combined with *in situ* measurements and model outputs, has
58 emerged as one of the best ways to detect regional trends in phytoplankton changes and
59 reveal a possible link with environmental forcing factors. The ocean color is referred to
60 spectrally resolved water-leaving radiance and inferred biogeochemical variables such as
61 Chlorophyll *a* (Chl *a*) concentration. Uncertainties in the retrieved ocean color data are
62 associated with atmospheric correction and in-water algorithms, and instrument performance.
63 Many studies have employed satellite-derived Chl *a* to assess a long-term trend associated
64 with environmental factors such as temperature and mixed layer depth that determine
65 phytoplankton phenology and primary production in high-latitude oceans (Kahru et al. 2011;
66 Lewis et al. 2020; Zhao et al. 2022). Despite these efforts, data gaps in ocean color products
67 stand out as a limiting factor for time-series analysis. Contaminated pixels caused by sun-
68 glint, sea ice, as well as persistent cloud cover significantly reduce the number of available
69 pixels that can be detected by satellite-based sensors (Blondeau-Patissier et al. 2014).

70 To fill the gaps caused by these issues, composite data is often generated using all
71 available values for a given period (e.g. 8-day mean) or by re-gridding data into a coarser
72 grid. Both strategies can help increase data coverage, however, it is still insufficient to
73 accurately determine the phenological metrics (Cole et al. 2012). The same problem remains
74 when multi-sensor merged products are employed, as the daily data coverage reaches only up
75 to 25% of the world ocean (Maritorena et al. 2010). The imperative search for broader
76 coverage and improved detection of both temporal and spatial variations of phytoplankton
77 biomass motivates further research into effective methods for interpolating missing data.

78 Data Interpolation Empirical Orthogonal Functions (DINEOF) is a classic technique to
79 reconstruct incomplete datasets on geophysical variables (Beckers and Rixen 2003). It is a
80 variant of learning algorithms that use matrix factorization to address missing data problems.
81 Thus, it has generally superior performance and accuracy over linear interpolation
82 (Ghahramani and Jordan 1993). Additionally, DINEOF is initially parameter-free, fast
83 convergent, and independent of a priori information, which permits its wide application to
84 geophysical datasets. Two most successful examples include satellite-derived data on sea
85 surface temperature (SST) and sea surface salinity (SSS) (Alvera-Azcárate et al. 2005;

This Work has been submitted to Journal of Atmospheric and Oceanic Technology.
Copyright in this Work may be transferred without further notice.

86 Alvera-Azcárate et al. 2007; Alvera-Azcárate et al. 2016). In contrast, its applicability to
87 biogeochemical variables (such as Chl *a*) is questionable given their high spatiotemporal
88 heterogeneity (i.e. a greater variance occurs in a small scale) in the upper ocean (Mahadevan
89 2005). Regardless, recent studies have applied DINEOF to recover missing data in Chl *a*
90 product. The impacts of missing data on reconstructed values are often ignored and there is
91 also a lack of sufficient validation (Hilborn and Costa 2018; Liu and Wang 2018, 2019;
92 Marchese et al. 2022).

93 This study proposes using DINEOF plus a masking procedure (hereafter referred to as
94 DINEOF+) that is applicable to an ocean color product based on a comprehensive basin-wide
95 evaluation across global oceans. We aim to provide conditions under which DINEOF+ can be
96 applied to recover missing ocean color data with statistical confidence by evaluating the
97 impacts of missing data on a global scale. Furthermore, as a proof of concept, we attempt to
98 apply DINEOF+ to reconstruct global satellite Chl *a* products to obtain high temporal
99 resolution ocean color dataset for advancing our knowledge about phytoplankton dynamics
100 including its phenology across the global ocean.

101 The paper is organized as follows: Section 2 describes the main steps of DINEOF+ and
102 provides additional information on its properties. The results of the evaluation are presented
103 in section 3, where we analyze the impacts of missing data. Section 4 presents the
104 reconstructed datasets on global daily Chl *a* after applying the method. Section 5 presents the
105 validation via comparison to *in situ* data. In section 6, we discuss the obtained results and
106 summarize the implications of our research study.

107 **2. Method**

108 *a. DINEOF algorithm*

109 Denote the data matrix \mathbf{A} whose entry $(i, j) \in [m] \times [n]$ corresponds to the observation
110 of the variable $f(r_i, t_j)$ at location r_i and moment t_j :

$$111 \quad \mathbf{A}_{ij} = f(r_i, t_j) \quad (1)$$

112 The empirical orthogonal functions (EOFs) can be calculated based on singular vector
113 decomposition (SVD) by solving:

$$114 \quad \mathbf{A}\mathbf{A}^T \mathbf{u} = \sigma^2 \mathbf{u} \quad (2)$$

115
$$\mathbf{A}^T \mathbf{A} \mathbf{v} = \sigma^2 \mathbf{v} \quad (3)$$

116 where u and v are referred to as spatial and temporal EOFs, respectively. σ represents
 117 singular value.

118 Thus, the initial matrix can be decomposed as:

119
$$\mathbf{A} = \sum_{i=1}^r \sigma_i \mathbf{u}_i \mathbf{v}_i \quad (4)$$

120 where $r = \text{rank}(\mathbf{A}) \leq \min(m, n)$.

121 In situations where \mathbf{A} is incomplete, the unknown entries \mathbf{A}_{ij}^u are estimated by using the
 122 truncated series of the first k EOFs, $\sum_{i=1}^k \sigma_i \mathbf{u}_i \mathbf{v}_i$. Then the EOFs are recalculated to update
 123 the previous estimations of the missing data. The main steps of DINEOF algorithm are
 124 summarized in Table 1.

125 Table 1. Summary of the main steps of DINEOF.

Algorithm DINEOF

1. Set the initial value \mathbf{X}_{ij}^0 for unknown entries \mathbf{A}_{ij}^u
 2. **For** each number of EOFs k **do**
 3. **while** in the t^{th} iteration of using k number of EOFs **do**
 4. Fill \mathbf{A} by replacing unknown entries \mathbf{A}_{ij} with \mathbf{X}_{ij}^{t-1} , denote the filled matrix as \mathbf{A}^t
 5. Compute the top k singular vectors \mathbf{u}_i , \mathbf{v}_i , and singular values σ_i of \mathbf{A}^t
 6. $\mathbf{X}_{ij}^t = \sum_{i=1}^k \sigma_i \mathbf{u}_i \mathbf{v}_i$
 7. **end while**
 8. **end for**
-

126
 127 More detailed procedures have been described in previous studies (Alvera-Azcárate et al.
 128 2005; Beckers and Rixen 2003; Liu and Wang 2019; Zhao 2023). However, we realize that
 129 there is a lack of explanation in terms of several important properties (e.g. convergence).
 130 Here, we provide some theoretical foundation for this algorithm:

131 (1) Convergence

132 The principle of DINEOF is equivalent to maximum likelihood estimation (MLE) for
133 solving a latent-variable model. The iteration of SVD with missing values can be expressed
134 by the Expectation-Maximization (EM) procedure, which ensures convergence (Sheng et al.
135 2005) assuming that the spatiotemporal data matrix is represented by a k -rank linear model
136 plus noise with a Gaussian distribution (see Appendix B).

137 (2) Initial values X_{ij}^o

138 DINEOF relies on pre-imputation to fill in missing data for implementing SVD. To have
139 an unbiased estimation, imputation by the average of the matrix provides better performance
140 than that by zeros and column-based average (Kurucz et al. 2007). In practice, the average is
141 subtracted during the entire process, so the missing data is initially assigned with zeros. We
142 notice that the use of a log-transformed matrix will improve the accuracy of recovered Chl a
143 data.

144 (3) Optimal number of EOF

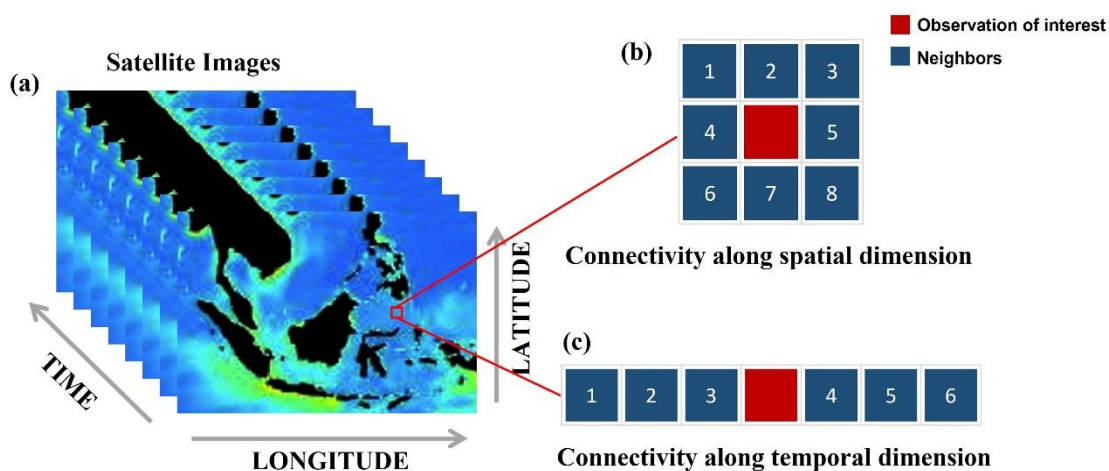
145 While k is fixed in each iteration, most algorithms choose to increase k as the
146 iteration proceeds until a local optimal result is achieved or it reaches a maximum
147 number. As an unsupervised process, the optimal number of EOF may vary each time
148 due to the random selection of samplings for cross-validation. It should be noted that
149 the process tends to be overfitted as the number of EOFs increases, resulting in
150 reduced accuracy of recovered elements (Yang et al. 2023).

151 *b. Connectivity mask*

152 Ocean color data is often characterized by a large number of missing data that are
153 unevenly distributed along both spatial and temporal dimensions. This results in
154 unpredictable errors in the reconstructed matrix. To improve the accuracy of DINEOF
155 reconstruction, this study proposes using DINEOF and then adding a connectivity mask,
156 which is explained below:

157 Based on the principle that DINEOF utilizes information along two dimensions (i.e. time
158 and space in satellite data; see Figure 1a) to reconstruct missing values, two conditions are
159 examined to identify those pixels that are unrecoverable: (1) spatial connectivity and (2)
160 temporal connectivity. If there is at least one observed value neighboring the pixel along a
161 spatial dimension, the pixel is defined as spatially connected. Similarly, the pixel is defined
162 as temporally connected when there is at least one neighboring pixel observed along the

163 temporal dimension. The pixels that are neither spatially nor temporally connected are
 164 removed from the final reconstructed matrix. In our study, the spatial connectivity is set as a
 165 neighboring structure of size 8 (Figure 1b), and the temporal connectivity is set as a
 166 neighboring structure of size 6 (Figure 1c).



167
 168 Fig. 1. Illustration of connectivity mask method. (a) Data structure of time-series satellite
 169 images; (b) 8-neighbor structure of connectivity along spatial dimension; (c) 6-neighbor
 170 structure of connectivity along temporal dimension.

171 *c. DINEOF+*

172 The main steps of DINEOF+ are summarized below:

173 Step 1) Organize sequences of selected images into a 2-D matrix \mathbf{X}_o where each column
 174 represents measurements on a particular day and each row is a time series of measurements at
 175 a pixel location.

176 Step 2) Subtract an average value from \mathbf{X}_o and set aside randomly at least 30 data points
 177 for cross-validation to determine the optimal number of EOFs. Meanwhile, all missing values
 178 are initialized as zero.

179 Step 3) If the PMD of \mathbf{X}_o is greater than 75%, remove some columns and rows until PMD
 180 is equal or less than 75%.

181 Step 4) Calculate the EOF series by using SVD of \mathbf{X}_o .

182 Step 5) Starting from $N = 1$, update missing data with truncated EOF series which
 183 consists of the first N EOFs

184 Step 6) Repeat steps (4)–(5) until convergence occurs and then calculate error
 185 estimations.

186 Step 7) Increase the number of EOFs until the error estimation begins to increase.

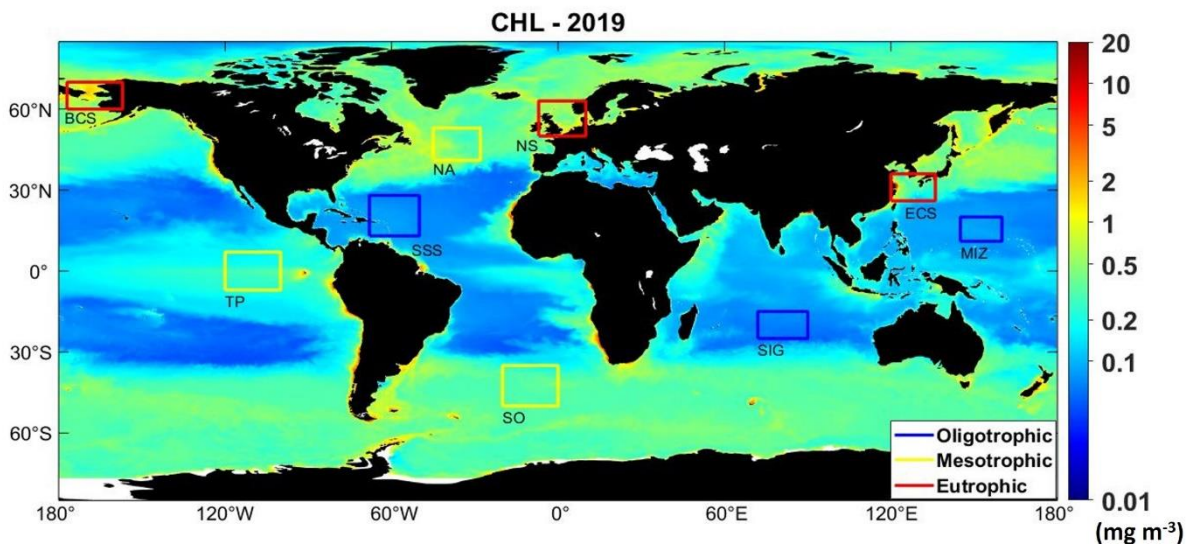
187 Step 8) Apply connectivity mask to the updated matrix.

188

189 3. Evaluation of impacts of missing data

190 a. Test data

191 The global daily chlorophyll concentration in 2019 at $0.25^\circ \times 0.25^\circ$ is obtained from
192 Copernicus Marine Services (<https://marine.copernicus.eu/>). It is derived from PISCES
193 biogeochemical model on the NEMO (version 3.6) platform (Aumont et al. 2015). To
194 evaluate impacts of the variance of Chl *a* magnitude on the performance of DINEOF+, the
195 datasets are selected from nine testing areas each with different trophic levels defined by their
196 range of Chl *a* (Antoine et al. 1996). This is comprised of three oligotrophic regions ($\text{Chl} \leq$
197 0.1 mg m^{-3}), three mesotrophic regions ($0.1 < \text{Chl} \leq 1 \text{ mg m}^{-3}$), and three eutrophic regions
198 ($\text{Chl} > 1 \text{ mg m}^{-3}$) (Figure 2, Table 2). These datasets are used in three ways: 1) Find the
199 threshold of missing data for applying DINEOF, 2) Determine the impact of the distribution
200 of missing data on the performance of DINEOF, and 3) Evaluate the performance of
201 DINEOF+.



202

203 Fig. 2. Global map of annual Chl *a* concentration from NEMO-PISCES model in 2019.
204 Testing areas include 3 oligotrophic regions (blue boxes), 3 mesotrophic regions (yellow
205 boxes orange), and 3 eutrophic regions (red boxes).
206

207 Table 2. Statistics of Chl *a* magnitude in testing areas from the global daily dataset in 2019.
208 Notes: Mean is the average value; STD is the standard deviation, *n* is row number along
209 latitude, *m* is column number along longitude, *t* is number of days for one year.

Regions	Size (<i>n</i>*<i>m</i>*<i>t</i>)	Mean (mg m⁻³)	STD (mg m⁻³)
Oligotrophic			
South Sargasso Sea (SSS)	71 * 59 * 365	0.0799	0.0111
Southern Indian Gyre (SIG)	71 * 39 * 365	0.0687	0.0115
Mariana Island Zone (MIZ)	59 * 35 * 365	0.0853	0.0117
Mesotrophic			
North Atlantic (NA)	67 * 47 * 365	0.4093	0.2977
Southern Ocean (SO)	79 * 59 * 365	0.3052	0.0993
Tropical Pacific (TP)	79 * 55 * 365	0.2288	0.0628
Eutrophic			
East China Sea (ECS)	63 * 39 * 365	0.4931	0.9193
Bering-Chukchi Sea (BCS)	79 * 39 * 365	0.8947	0.9561
North Sea (NS)	67 * 51 * 365	0.6844	0.6017

210

211 *b. Threshold of the percentage of missing data*

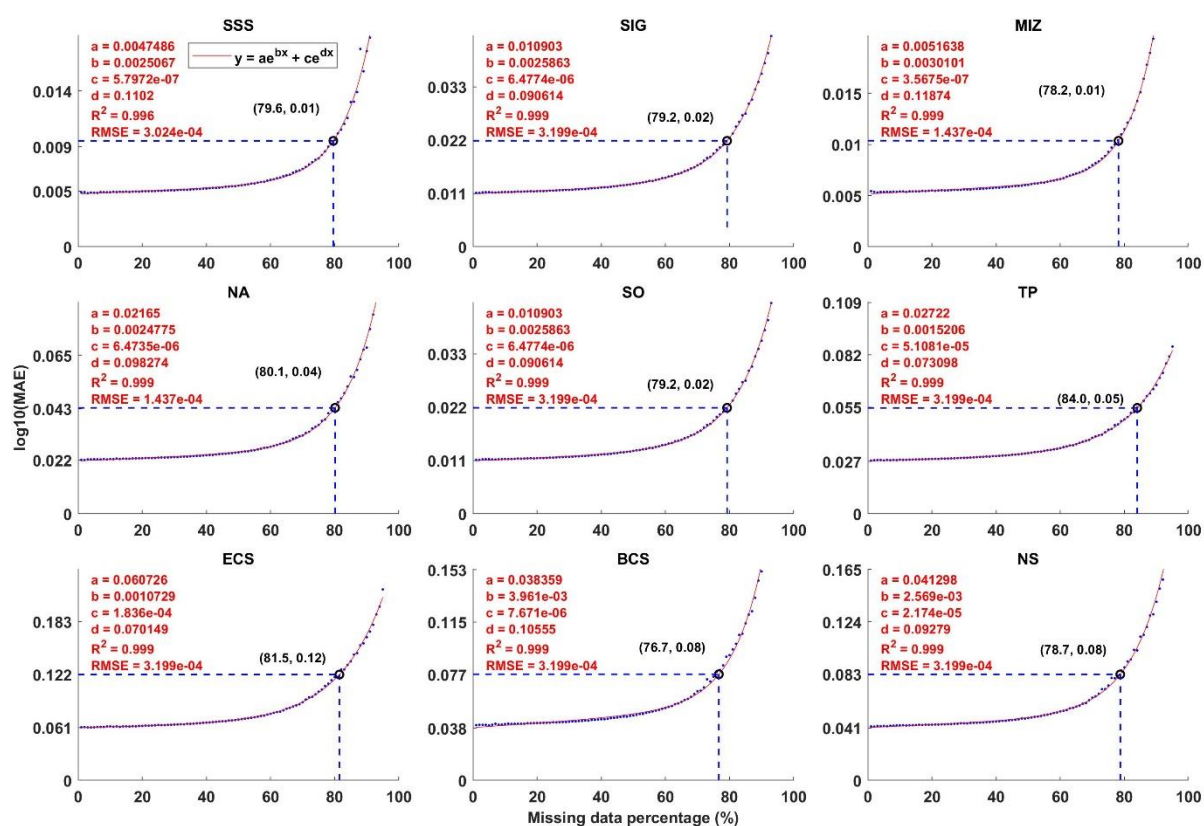
212 We first prepare the data matrix, \mathbf{A}^o , by randomly removing 1% of the pixels from the
213 original data and then generate a reconstructed dataset. We repeat this procedure by removing
214 an additional 1% of the original pixels through several iterations until 95% of the data is
215 removed to assess the impact of missing data on reconstructed results derived by DINEOF+.
216 Selected error metrics for algorithm evaluation include bias, median absolute error (MAE)
217 (Eq. (5) and Eq. (6)), root mean square error (RMSE), regression slope, and r^2 . All data
218 values are log-transformed prior to the calculation of the error metrics.

219
$$\text{bias} = 10^{\text{median}(\log_{10}(\mathbf{M}_i) - \log_{10}(\mathbf{O}_i))} \quad (5)$$

220
$$\text{MAE} = 10^{\text{median}(|\log_{10}(\mathbf{M}_i) - \log_{10}(\mathbf{O}_i)|)} \quad (6)$$

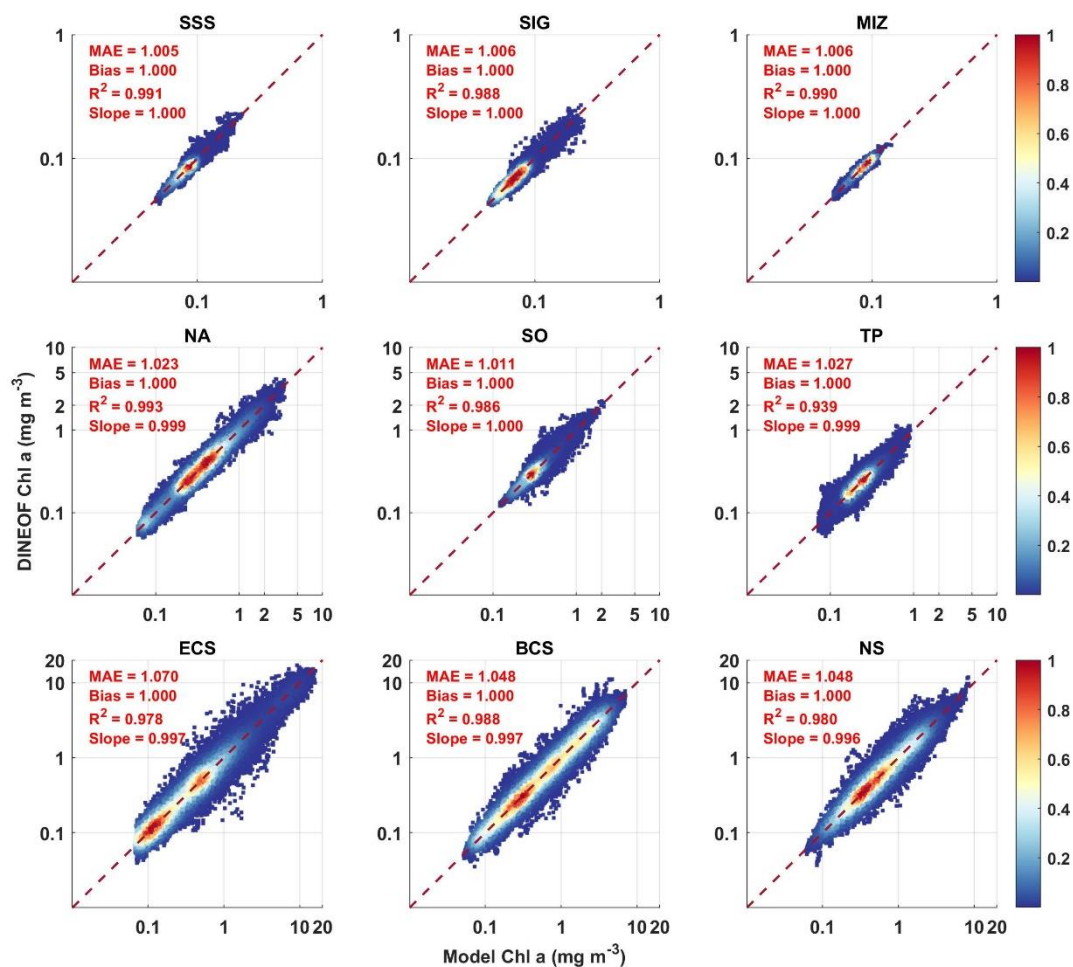
221 Where \mathbf{O}_i is the model value as reference solution, \mathbf{M}_i is the estimated value, $i = 1, 2, \dots, n$
 222 and n is the extent of missing data.

223 Here, we select MAE as the representative error metric. Figure 3 shows the errors
 224 consistently increase with the percentage of missing data (PMD) in all testing areas. In
 225 oligotrophic regions, the magnitude of errors ranges from 1.005 to 1.04 when the PMD
 226 increases from 1–95%. In the mesotrophic and eutrophic regions, the ranges are 1.01–1.10%
 227 and 1.04–1.24% respectively. We found the two-term exponential model fits the trends of
 228 MAE with r^2 above 0.99 for all testing areas. It predicts that the PMD is 76–84%, when \log_{10}
 229 transformed error (the exponent in (6)) is doubled (i.e., MAE is squared).



230
 231 Fig. 3. Scatterplots of $\log_{10}(\text{MAE})$ vs. percentage of missing data (PMD). The trendline
 232 (red line) is described by a two-term exponential model. The black circle indicates the value
 233 of PMD when the \log_{10} -transformed error (the exponent in (6)) is doubled (i.e., MAE is
 234 squared).

235
 236 To evaluate the performance using other metrics, we recreate a data matrix with 75% of
 237 missing data in each testing area. The results show r^2 is above 0.9, bias and slope are all
 238 around 1 (Figure 4). Based on these evaluations, we determine that 75% is a safe threshold
 239 as the percentage of missing pixels, where the DINEOF is reasonably applied.



240

241 Fig. 4. Scatterplot of DINEOF reconstructed Chl *a* vs original model value. The
242 percentage of missing data is 75% for all testing areas. The color represents data density. Red
243 line = 1:1 ratio.

244

245 *c. Impact of the distribution of missing data and validation of DINEOF+*

246 To evaluate the impacts of the temporal and spatial distribution of missing data, a mask is
247 created based on the global daily L3 MODIS-Aqua CHL product in 2019. The mask is
248 applied to the model-derived Chl *a* so that incomplete dataset can have the same sparsity
249 pattern as observed in the real satellite data.

250 Compared to random distribution, the gaps derived from satellite data result in higher
251 MAE of reconstructed data in all testing areas when PMD are the same (Table 3). The
252 increases of MAE in the mesotrophic and eutrophic regions are generally one magnitude
253 greater than in the oligotrophic regions. In addition, the mean square error of initial

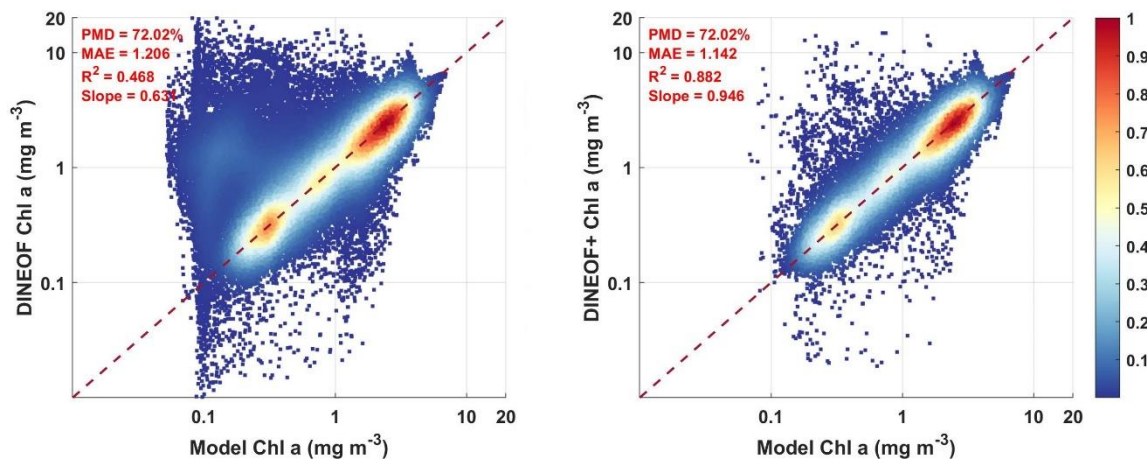
254 incomplete data does not show any correlation to the MAE. Therefore, we assert that the
 255 increased error is attributed to the difference in sparsity patterns.

256 Table 3. Statistic of data reconstruction in testing areas when the missing data is distributed in
 257 random and real satellite data in 2019. $\|\cdot\|_F$ denote Frobenius norm. * indicates that the
 258 calculation is based on log10-transform.

Testing areas	PMD (%)	Gaps in random		Gaps as in satellite data	
		$\ \Delta\ _F^2/n$	MAE*	$\ \Delta\ _F^2/n$	MAE*
SSS	66.95	0.004	1.004	0.004	1.007
SIG	70.62	0.003	1.006	0.003	1.008
MIZ	72.23	0.005	1.006	0.005	1.011
NA	87.51	0.226	1.038	0.228	1.072
SO	85.20	0.088	1.015	0.087	1.034
TP	75.56	0.043	1.027	0.041	1.048
ECS	82.94	0.621	1.092	0.691	1.163
BCS	82.19	2.195	1.091	1.915	1.245
NS	74.32	0.671	1.052	0.645	1.106

259

260 Furthermore, we selected the test data of the BCS as an example to analyze the
 261 characteristics of the distribution of missing data and errors in the reconstructed matrix. After
 262 removing null rows and columns, the overall PMD is 72.02%. The missing data is unevenly
 263 distributed in the data matrix where the column-based PMD ranges from 0.03 to 52.19%
 264 (Figure 5a). This is consistent with the fact that persistent cloud cover results in a large
 265 percentage of missing data in some areas during a year. The absolute error matrix shows a
 266 great variance of errors in the reconstructed missing data (Figure 5a). Large errors are
 267 highlighted in red and yellow color between the row 1600 and row 1200. The r^2 and slope are
 268 reduced to 0.508 and 0.683 respectively (Figure 5b) compared to 0.998 and 0.997 when the
 269 missing data is randomly distributed (Figure 4). After the use of the connectivity mask, these
 270 pixels of large errors are successfully identified and removed from the reconstructed matrix
 271 (Figure 5c), and thus significantly improve the overall accuracy (Figure 5d).

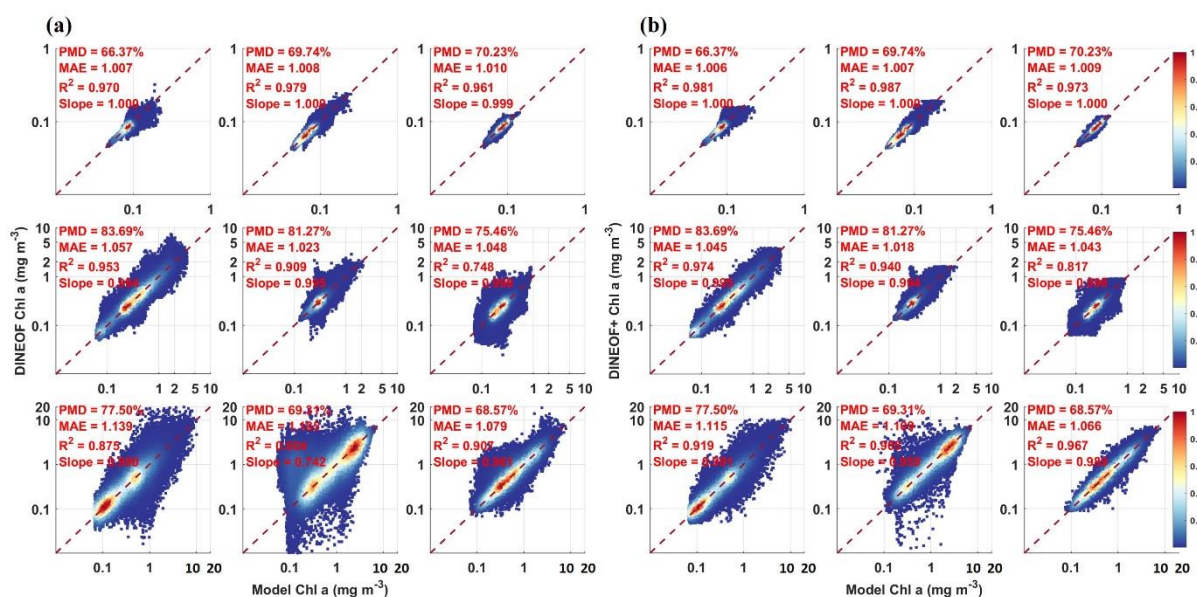


272

273 Fig. 5. DINEOF reconstructed data vs original model value before (b) and after (d)
 274 connectivity mask is applied in the BCS. The color indicates data density. Red line = 1:1
 275 ratio. Values are log-transformed prior to the calculation of errors. White indicates no data.

276

277 We compared the results of all test areas reconstructed by DINEOF with and without
 278 connectivity mask (Figure 6). Measured by r^2 , MAE, and slope, the performance of DINEOF
 279 is least affected by missing data in three oligotrophic regions (Figure 6a). In the TP, ECS and
 280 BCS, the r^2 is below 0.9. It is obvious that the effect of gaps in real satellite data decreases the
 281 accuracy of reconstructed data particularly in the eutrophic regions. After the use of
 282 connectivity mask, the r^2 increased from 0.752 to 0.823 in the TP, from 0.883 to 0.923 in the
 283 ECS and from 0.419 to 0.896 in the BCS. MAE and slope are also improved in all test areas
 284 (Figure 6b).



285

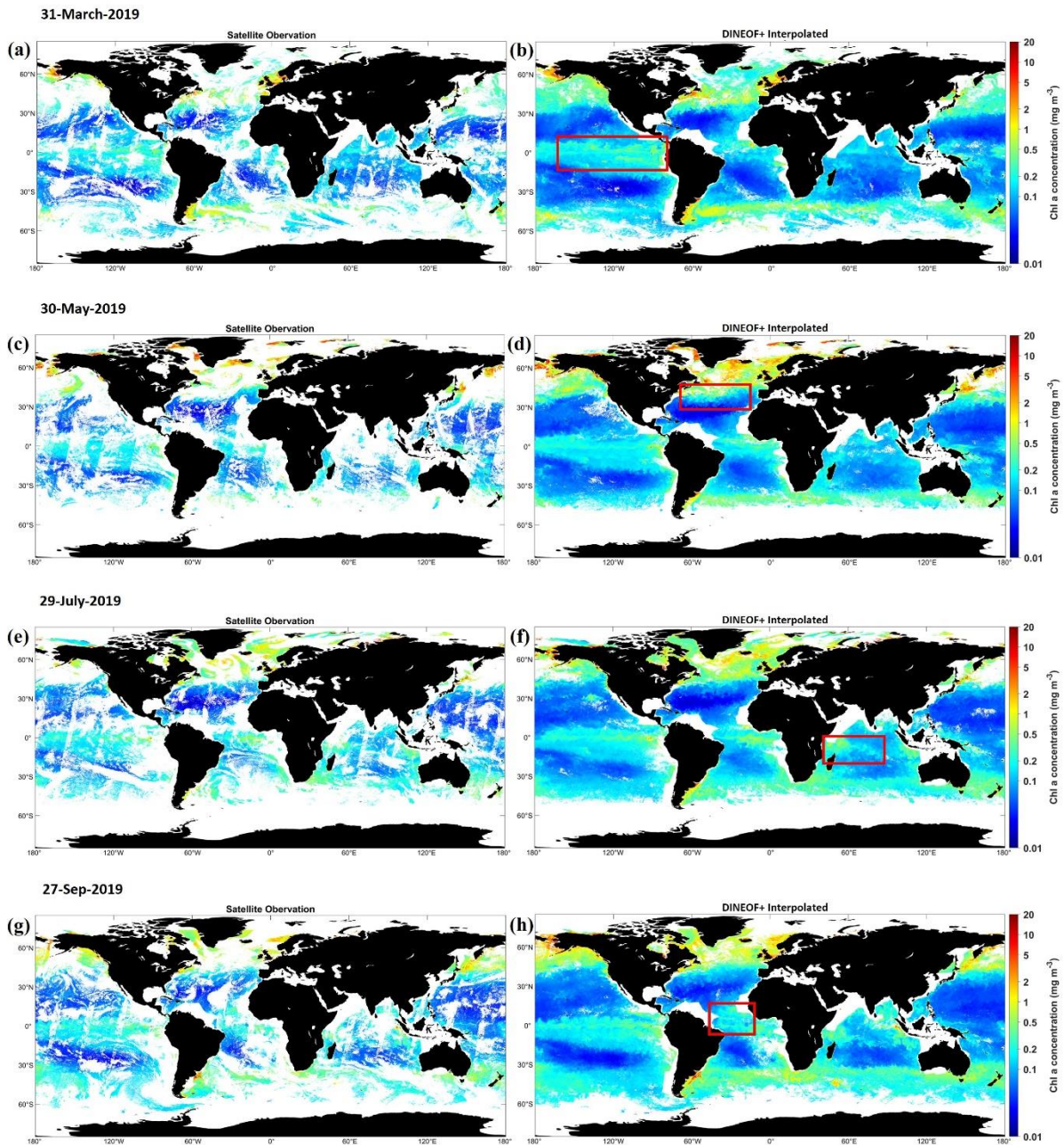
286 Fig. 6. Scatterplot of DINEOF reconstructed Chl *a* and original model value before (a)
287 and after (b) connectivity mask is applied. The distribution of missing data has the same
288 temporospatial pattern as daily L3 MODIS-Aqua Chl *a* product in 2019 where the mask was
289 obtained. The minimum percentage of missing data is 6% in each column and row. The color
290 indicates data density. Red line = 1:1 ratio.

291

292 **4. Application to OC-CCI global daily Chl *a* product**

293 To demonstrate how DINEOF+ behaves on real satellite data, we now use a multi-sensor
294 dataset in 2019 obtained from the ESA Ocean Color Climate Change initiative (OC-CCI)
295 (<https://www.oceancolour.org/>) (Sathyendranath et al. 2019). It consists of 365 days' images
296 at 4 km resolution over the global ocean. In this study, we exclude coastal waters and
297 delineate the open ocean into 21 subregions based on the biome boundaries (Figure A1).
298 There are 2.88–11.27% of available pixels in the 7 polar biomes including the Baffin Bay,
299 Greenland Sea, Hudson Bay, Kara Sea, Laptev Sea, Pacific Arctic and Southern Ocean south
300 of 60°S latitude (Table A1), 12.15–18.86% of data availability in the subpolar waters of
301 North Atlantic, North Pacific and Southern Ocean, and 30.22–49.95% in oceans between
302 40°N–50°S mainly composed of oligotrophic waters.

303 As seen from the four sequenced images (Figure 7a, c, e, g), missing data is nonuniformly
304 distributed across different ocean basins and dates. A consistently large number of missing
305 data is found in the high-latitude regions including the North Atlantic, North Pacific and
306 Southern Oceans. Consequently, it is almost impossible to detect the development of
307 phytoplankton blooms in these regions throughout the year. By applying the DINEOF+ to
308 this data, it is shown that clear spatial patterns of Chl *a* distribution are obtained in the
309 reconstructed images (Figure 7b, d, f, h). Noticeable spring blooms are observed in the
310 Bering-Chukchi Sea, North Atlantic and Southern Oceans. Meanwhile, high Chl *a*
311 concentrations are shown distributed along the equatorial Atlantic and eastern Pacific all year
312 around. In September, a second bloom can be observed in the North Pacific and Atlantic
313 Oceans (Figure 7h). Within these mesoscale structures, there are some sub-mesoscale
314 features such as filaments and eddy-shaped Chl *a* blooms (Figure b, d, f, h) which are not
315 visible in the original dataset due to the presence of gaps. The availability of daily data
316 increases by 51% in the equatorial Pacific and Atlantic, and 43–55% in the oligotrophic
317 regions including the gyres north and south of the equator and Indian Ocean (Table A1).



318

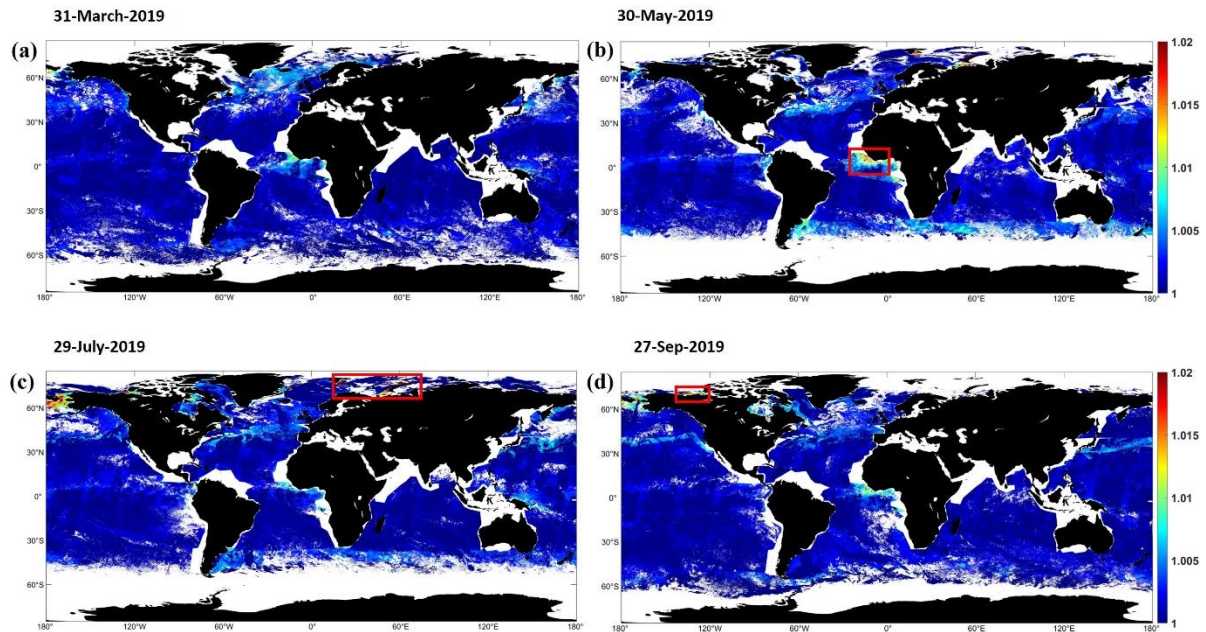
319 Fig. 7. Global daily Chl *a* concentration from level 3 daily ESA-CCI at 4 km resolution
 320 (left panels) and corresponding DINEOF+ reconstructed results (right panels) in 2019 on (a,
 321 b) March 31; (c, d) May 30; (e, f) July 29; (g, h) Sep 27. The red boxes indicate areas with
 322 sub-mesoscale features such as eddies and filaments. White color indicates no data.

323 Error maps associated with the reconstruction are given by using the method proposed by
 324 (Beckers et al. 2006). The expected error, ϵ at a given location \mathbf{r} is defined as:

325
$$\epsilon(\mathbf{r}) = 10^{RMS(\log_{10}(\varphi(\mathbf{r})) - \log_{10}(\varphi_t(\mathbf{r})))} \quad (7)$$

326 Where RMS is root mean square, $RMS(x_i) = \sqrt{\frac{\sum_{i=1}^n x_i^2}{n}}$, φ is the interpolated field and φ_t
327 is the true field.

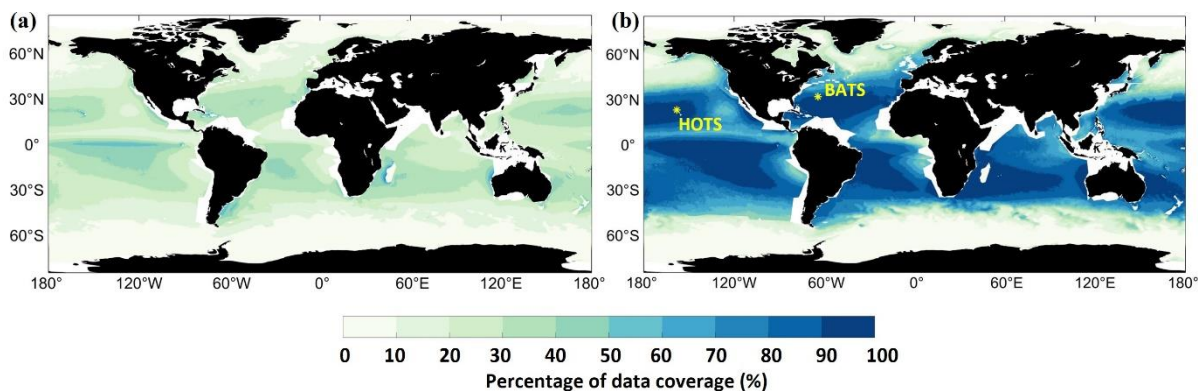
328 We use an error length of 29 km. The value of expected error ranges from 1 to 1.02 with
329 exceptions of some points that reach 1.04 - 1.05 in the polar waters (Figure 8). Since the
330 errors are within the range of regional MAE estimated from our validation, no further
331 removal of points seems necessary.



332
333 Fig. 8. The estimated error (Eq. 7) for the DINEOF+ reconstruction in 2019 on (a) March
334 31; (b) May 30; (c) July 29; (d) Sep 27. The red boxes indicate areas with relatively higher
335 error. Values are log-transformed prior to the calculation of errors. White color indicates no
336 data.

337
338 In addition to 2019, we also applied DINEOF+ to the global daily datasets from 2003 to
339 2020 for further confirming improvements on Chl a time series observation. The annual mean
340 coverage of daily data on Chl a is 22.5% in the equatorial Atlantic, 28.92% in the equatorial
341 Pacific, 11.77% in the subpolar North Atlantic, 12.62% in the subpolar North Pacific, 28.08%
342 in the oligotrophic oceans and 4.49% in the polar oceans (Figure 9a). After we applied the
343 method, the annual mean coverage increases to 60.9% in the equatorial Atlantic, 76.65% in
344 the equatorial Pacific and 76.78% in the oligotrophic oceans (Figure 9b), though the
345 availability of daily Chl a is still below 20% in subpolar and polar oceans. In the next section,
346 we compare the reconstructed Chl a to *in situ* observations including two times-series data

347 from Bermuda Atlantic Time-series Study (BATS) and Hawaii Ocean Time-series Station
348 (HOTS). Both stations are located in the oligotrophic region where the annual mean data
349 coverage reaches 76% in the reconstructed datasets (Figure 9b).



350

351 Fig. 9. Annual mean coverage of daily Chl *a* data during 2003–2020: (a) level-3 daily
352 ESA-CCI at 4 km resolution; (b) Corresponding DINEOF reconstructed results. The data
353 coverage is the percentage of available data in each pixel with regard to the total number of
354 time steps. The location of BATS and HOTS are marked as asterisk in panel (b).

355

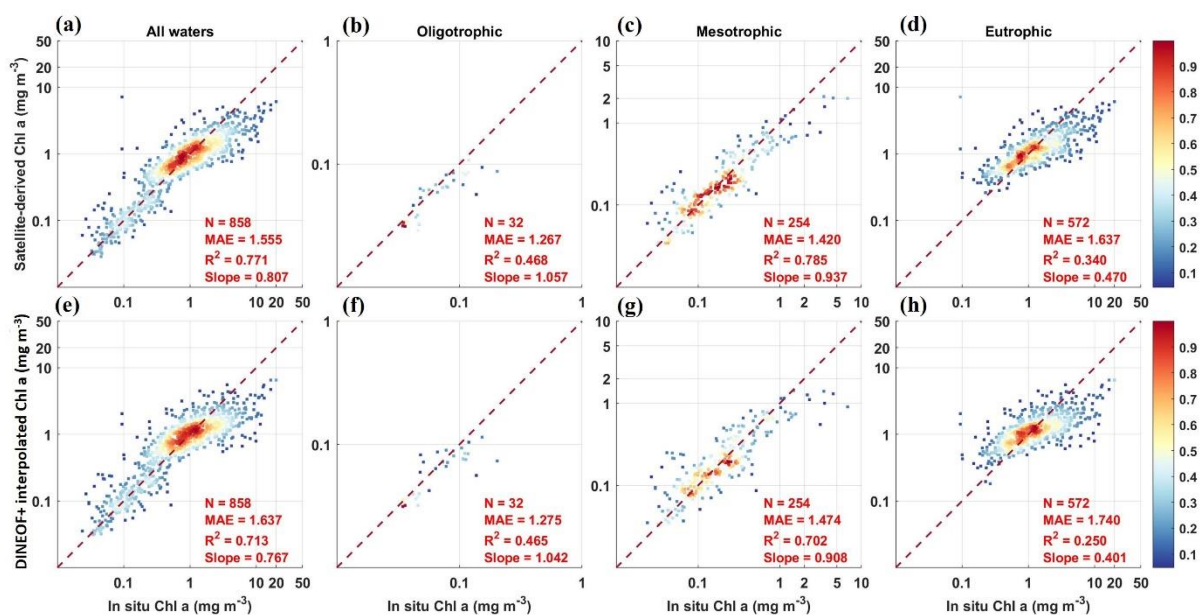
356 5. Validation: match-ups with *in situ* data

357 In this section, we perform validation of DINEOF+ interpolated Chl *a* via comparisons to
358 *in situ* measurements. The *in situ* measurements are selected from SeaBASS during 2003–
359 2020 (<https://seabass.gsfc.nasa.gov/>) that includes both fluorometric and HPLC-derived Chl
360 *a*. The coincident satellite pixels are removed from datasets and are recovered by applying
361 DINEOF+. The total number of matchups used for validation between *in situ* and
362 reconstructed pixels is 858 located across the global ocean (Figure A2). Furthermore, we
363 divide these matchups into oligotrophic, mesotrophic, and eutrophic waters according to the
364 definition used in section 3.

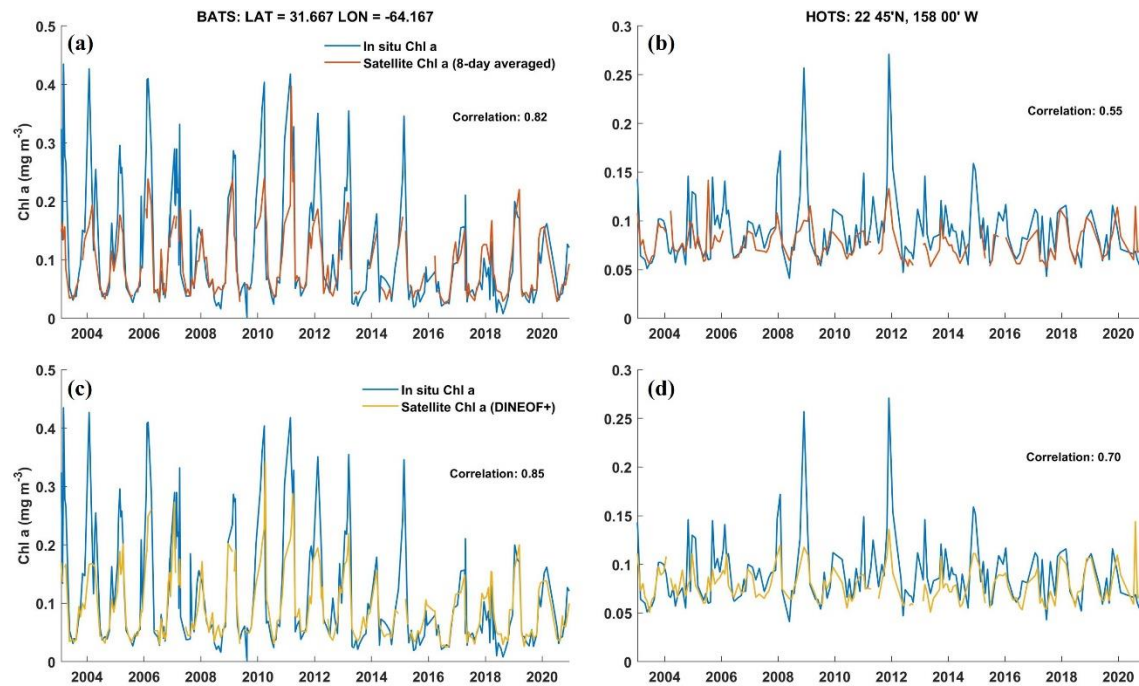
365 Measured by MAE, r^2 and slope, the errors of DINEOF+ interpolated Chl *a* are
366 quantitatively similar to the original satellite-derived Chl *a* across all waters (Figure 10a, e).
367 DINEOF+ performs poorest in the eutrophic indicated by the r^2 and MAE (Figure 10h).
368 However, similar error metrics are also found in the original satellite-derived Chl *a* (Figure
369 10d). Thus, we posit that the errors are mostly inherent differences between satellite-derived
370 Chl *a* and *in situ* measurements. A similar performance is also shown in the oligotrophic
371 (Figure 10b, f) and mesotrophic areas (Figure 10c, g). Although DINEOF+ reconstruction

372 added noise to the original pixel values, it also helps reduce the error of abnormal
 373 measurements in the datasets as shown in our examples (Figure 10a, c and Figure 10d, h).

374 Figure 11 allows a comparison of *in situ* surface Chl *a* (SChl *a*) evolution (blue curve)
 375 with the satellite retrieved concentrations on the 8-day average (red curve) and DINEOF+
 376 daily resolution (yellow curve) over their overlapping period during 2003–2020. It shows that
 377 both satellite and DINEOF+ derived signals agree well with the *in situ* observations of SChl *a*
 378 at BATS in terms of seasonal pattern, annual variation and magnitude. At HOTS, SChl *a*
 379 concentration is underestimated by the coincident satellite measurements over the periods
 380 while the DINEOF+ daily time series exhibit a better agreement with the *in situ* SChl *a*
 381 indicated by a higher correlation coefficient (Figure 11b, d). Furthermore, the DINEOF daily
 382 time series includes more measurements within a weekly scale (Figure 3A) and thus provides
 383 reasonable Chl *a* evolution such as the timing of bloom peaks.



384
 385 Fig. 10. Scattering plots of original satellite-derived vs *In situ* Chl *a* (top panel) and
 386 DINEOF+ interpolated vs *In situ* Chl *a* (bottom panel): (a, e) Across all water types, (b, f)
 387 Oligotrophic, (c, g) Mesotrophic, (d, h) Eutrophic. N is the number of match-ups. Red line =
 388 1:1 ratio.



389

390 Fig. 11. Comparison of *in situ* surface Chl *a* time series (blue curves) to 8-day average
391 ESA OC-CCI Chl *a* time series (red curves) and DINEOF+ interpolated Chl *a* time series
392 (yellow curves). The *in situ* measurements are located at BATS (a, c) and HOTS (b, d).

393 6. Discussion

394 Due to persistent gaps in satellite observations, it is challenging to interpret
395 phytoplankton dynamics in time and space using ocean color data. Previous studies have
396 shown that the DINEOF algorithm is an effective method for recovering missing data of
397 geophysical variables such as SST and SSS. In this study, we propose an enhanced DINEOF
398 algorithm (i.e. DINEOF+) and provide a comprehensive validation of the reconstructed Chl *a*
399 by comparison to both simulated and *in situ* measurements.

400 Our validation confirms that both the total number and distribution pattern of missing
401 data are related to the accuracy of recovered missing data. According to the theory of matrix
402 completion, unknown entries from a matrix are not guaranteed to be recovered unless a
403 sufficient number of them are observed, and these samples are uniformly random (Candès &
404 Recht, 2009). This raises certain requirements for the datasets that need to be recovered. In
405 terms of the number of missing data, we show that 75% of PMD is a threshold for performing
406 DINEOF+. In real satellite images, data gaps are not uniformly distributed and the PMD
407 often reaches above 75% particularly in high latitude and coastal regions. It is useful to skip
408 some days and locations to reduce the overall PMD of a data matrix. Our validation also

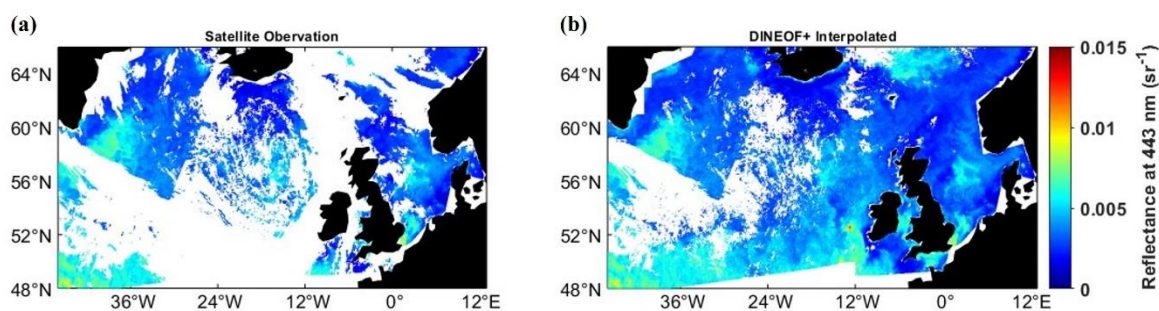
409 shows that the real data gaps will impair the accuracy of reconstructed values compared to
410 the tests based on random samplings (Table 3). Although we cannot define a quantitative
411 criterion to determine which distribution of gaps allows a data reconstruction, the
412 connectivity mask works as an effective method of removing highly biased values by
413 examining the condition of data availability neighboring each pixel since the physical
414 correlation with a valid neighbor is generally stronger than with a point much further away.
415 Users can change the size of neighboring structures (Figure 1) according to the study areas.
416 Future studies may consider designing a weighted structure using pixels of different length
417 scales.

418 In addition to missing data, the influence of variance or heterogeneity of the dataset also
419 needs to be considered for applying DINEOF+. In our experiments, we observed much higher
420 errors in the eutrophic regions (i.e., ECS, BCS, NS) compared to mesotrophic and
421 oligotrophic regions (Table 3). This indicates that the reconstruction of Chl *a* values will have
422 larger uncertainties in those regions that are characterized by greater variance in time and
423 space. Typical examples include most coastal oceans where Chl *a* is characterized by high
424 variance throughout a year (O'Reilly & Werdell, 2019). This implies the need for caution
425 when applying DINEOF+ to reconstruct Chl *a* in these regions. Nevertheless, DINEOF+
426 demonstrates its strength in recovering the development of phytoplankton blooms
427 characterized by a high spatial heterogeneity of Chl *a* concentration.

428 For global applications, previous studies simply divided the entire oceans into subareas
429 by latitude to increase the efficiency of implementing DINEOF (Liu & Wang, 2018, 2019).
430 Here, we argue that this is not an appropriate method regarding the high heterogeneity of Chl
431 *a* in the upper ocean. Fay and McKinley (2014) defined 17 open-ocean biomes classified
432 according to observations of Chl *a*, SST and MLD. Using these biomes provides a basis for
433 an alternative method applying DINEOF+ for reconstructing Chl *a* dataset. Our results
434 improve the daily Chl *a* coverage by 26.86% for the global open oceans during 2003–2020.
435 When using biomes-based reconstruction several properties need to be considered: first, it
436 excludes coastal regions which tend to have very high variance of Chl *a*; second the biomes
437 are classified based on biogeochemical functions and thus exhibit more consistent changes in
438 Chl *a* through a year; third, it provides a mean to apply and compare reconstructed datasets
439 for biome-scale studies on phytoplankton dynamics and primary production. It should be
440 noted that the recovery rate varies with ocean basins and years, depending on the data

441 availability in the original dataset. In the oligotrophic oceans between 40°N–40°S, the daily
442 Chl *a* coverage increased by 43–55% on average, which provides us with a nearly complete
443 daily Chl *a* time series at single pixel level for decades (Figure A3). In contrast, there is only
444 4.66% of the increase in the polar oceans. To obtain higher data coverage in high-latitude
445 oceans, we suggest applying DINEOF+ to a composite dataset such as 8-day running mean.

446 The potential applications of DINEOF+ extend beyond the specific dataset on Chl *a*.
447 Figure 12 illustrates an example of applying DINEOF+ to datasets on Remote Sensing
448 Reflectance (Rrs) at 443 nm. Using DINEOF+ greatly increased the data coverage of daily
449 Rrs product. As a fundamental parameter used in ocean color remote sensing, the
450 reconstructed Rrs product can be used to derive other ocean color datasets on parameters such
451 as Chl *a*, Colored Dissolved Organic Matter (CDOM), and Particulate Organic Carbon
452 (POC).



453
454 Fig. 12. Remote sensing reflectance at 443 nm in the North Atlantic Ocean from level 3
455 daily ESA-CCI product at 4 km resolution (left panels) and corresponding DINEOF+
456 reconstructed results (right panels) on 12 Sep 2022. White color indicates no data.

457 458 7. Concluding remarks

459 We demonstrate that DINEOF+ is a useful technique that allows us to obtain an
460 unprecedented high-temporal resolution ocean color dataset. Using this dataset will
461 unequivocally enhance our ability to interpret the natural variability of surface Chl *a*
462 concentration that is dominated by high-frequency fluctuations at small spatial scales
463 (Keerthi et al. 2022). Temporal resolution of the dataset also influences determining
464 phenological metrics of phytoplankton such as the timing of bloom initiation and peaks.
465 Because DINEOF+ can effectively increase the temporal resolution of Chl *a* time series for
466 one year it will reduce the uncertainty resulting from the original data gaps.

467

This Work has been submitted to Journal of Atmospheric and Oceanic Technology.
Copyright in this Work may be transferred without further notice.

468 *Acknowledgments.*

469 We thank ESA OC-CCI group for the data availability, production and maintenance for
470 the ocean color data used in this manuscript. We also thank the scientists and crewmembers
471 for running the BATS (NSF OCE-1756105 and OCE-2122606) and HOT Time-series project
472 over the last three decades. We thank four anonymous reviewers for their insightful
473 comments that help improve the manuscript.

474 Parts of this research were supported by NASA ROSES project (sponsor award
475 #210319602) and Japan Aerospace Exploration Agency (JAXA) Global Change Observation
476 Mission-Climate, GCOM-C (contracts #22RT000298) to AM.

477 *Data Availability Statement.*

478 This study has been conducted using E.U. Copernicus Marine Service Information;
479 <https://doi.org/10.48670/moi-00019> and <https://doi.org/10.48670/moi-00282>. Datasets from
480 HOTS and BATS are accessible through [https://hahana.soest.hawaii.edu/hot/hot-](https://hahana.soest.hawaii.edu/hot/hot-dogs/interface.html)
481 [dogs/interface.html](https://hahana.soest.hawaii.edu/hot/hot-dogs/interface.html) and <https://bats.bios.asu.edu/data/>.

482 The code of DINEOF+ used in this manuscript can be found in GitHub repository
483 <https://github.com/zhprm1992/DINEOF-plus.git>

484

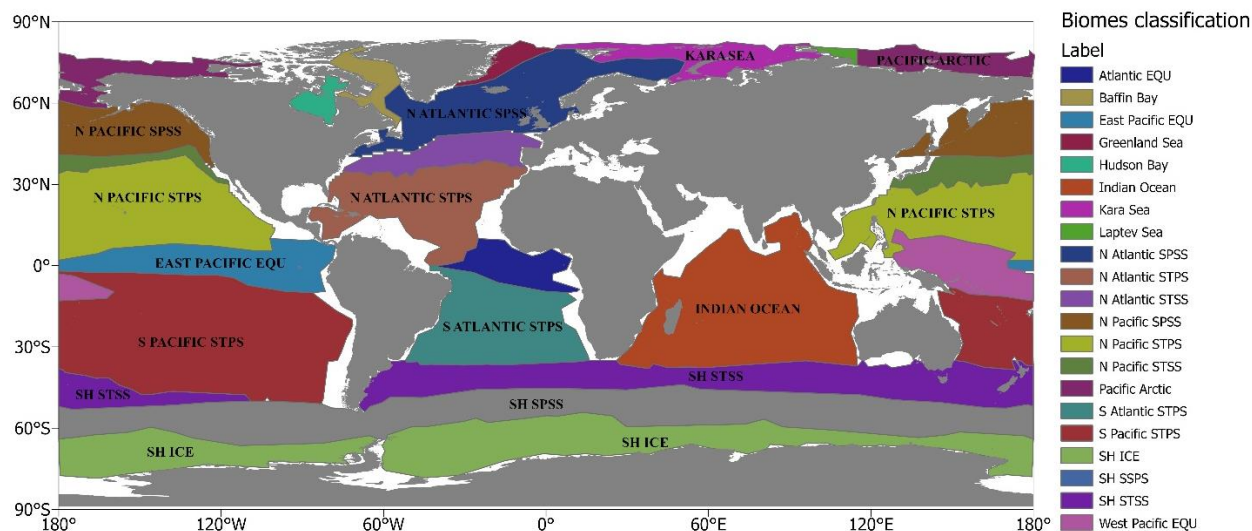
485

APPENDIX A

486

Application to global biomes and validation

487 In the study, we propose using biomes classification rather than latitudinal bands when
488 applying DINEOF+ to reconstruct the global Chl *a* dataset. The advantages of using this
489 approach are discussed in section 6. This section includes a map of 21 ocean biomes (Fig A1)
490 defined by Fay (2014) based on observations of Chl *a* and environmental variables such
491 mixed layer depth and sea surface temperature. We provide an example of the percentage of
492 available daily data in each biome in 2019 after applying DINEOF+ (Table A1). Fig A2
493 illustrates the geographic locations of all in situ data used for validation, as described in
494 section 5. Additionally, we present the complete time series of matchups between DINEOF+
495 interpolated daily Chl *a* and *in situ* data at the BATS and HOTS stations (Fig A3).



496

497 Fig A1. Global open-ocean biomes. The base map is created by Fay and McKinley
 498 (2014). ICE: ice biome; SPSS: subpolar seasonally stratified biome; SPSS: subtropical
 499 seasonally stratified biome; STPS: subtropical permanently stratified biome; EQU: equatorial
 500 biome. White indicated ocean areas that do not fit the criteria for any biome and are excluded
 501 from further analysis.

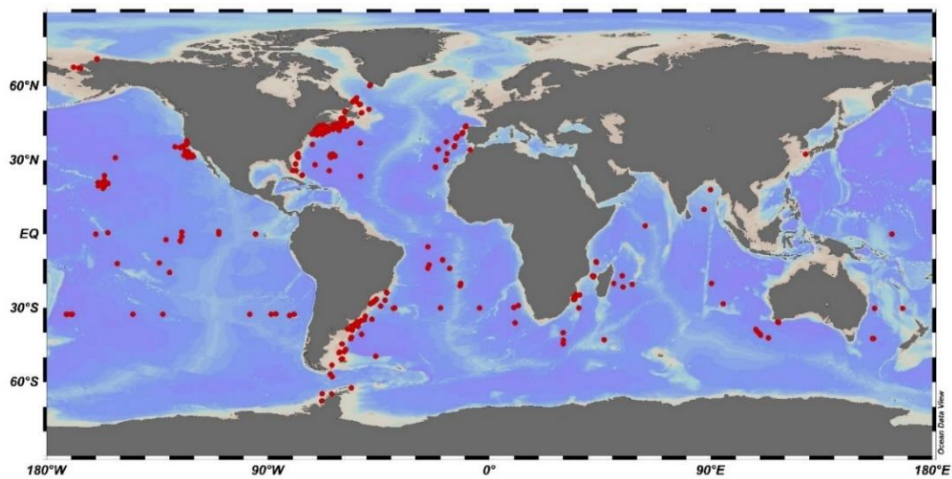
502

503

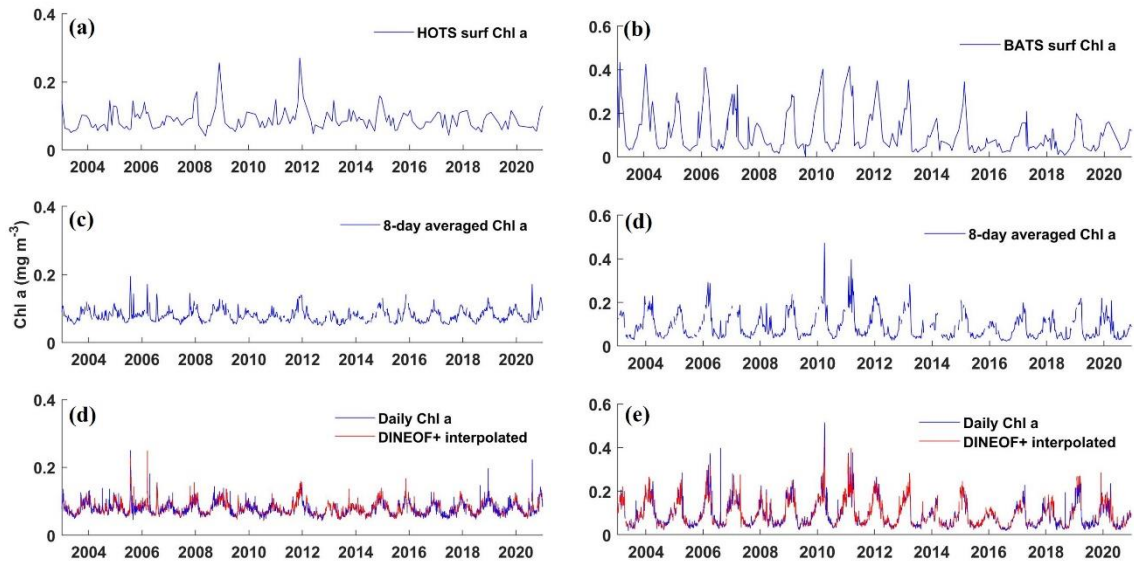
NO.		Daily Chl <i>a</i>	DINEOF daily Chl <i>a</i>	8-day Chl <i>a</i>
1	Atlantic EQU	43.55%	94.59%	95.27%
2	N Atlantic STPS	54.05%	97.53%	97.81%
3	N Atlantic STSS	32.82%	86.02%	86.44%
4	Baffin Bay	11.27%	27.90%	31.45%
5	E Pacific EQU	49.95%	95.30%	95.57%
6	Greenland Sea	4.77%	8.97%	17.21%
7	Hudson Bay	8.85%	20.89%	25.35%
8	Indian Ocean	48.95%	95.10%	95.52%
9	Kara Sea	4.55%	7.40%	16.91%
10	Laptev Sea	2.88%	3.80%	11.54%
11	N Atlantic SPSS	14.99%	38.45%	51.77%
12	N Pacific SPSS	18.86%	48.95%	65.69%

13	Pacific Arctic	4.91%	8.58%	17.60%
14	N Pacific STPS	47.32%	95.10%	95.63%
15	N Pacific STSS	30.22%	85.34%	86.03%
16	S Pacific STPS	42.84%	91.81%	92.48%
17	SH ICE	3.28%	3.60%	15.70%
18	S Atlantic STPS	48.84%	95.37%	95.89%
19	SH SPSS	12.15%	26.90%	49.04%
20	SH STSS	27.51%	79.51%	80.47%
21	W Pacific EQU	40.61%	92.02%	93.07%

504 Table A1. The percentage of available daily Chl *a* pixels in each biome in 2019.
 505



506
 507 Fig A2. Geographic locations of in situ datasets used for validation of DINEOF
 508 reconstruction. Red dots are *in situ* Chl *a* measurements retrieved from SeaBASS.
 509



510

511 Fig A3. Chl *a* time series from 2003 to 2020. Left panels are HOTS *in situ* surf Chl *a* (a),
 512 and satellite matchup of 8-day average Chl *a* (c) and DINEOF-interpolated daily Chl *a* (d).
 513 Right panels are BATS *in situ* surf Chl *a* (b), and satellite matchup of 8-day average Chl *a* (d)
 514 and DINEOF+ interpolated daily Chl *a* (e).

515

516

APPENDIX B

517

The theoretical foundation for convergence properties of DINEOF

518

DINEOF can be regarded as an approach of using maximum likelihood estimation (MLE)

519

to solve a latent-variable model. The iteration of SVD is essentially a practical application of

520

the Expectation-Maximization (EM) algorithm when we assume the original incomplete data

521

matrix can be represented by a linear model plus noise with a Gaussian distribution.

522

This section provides the theoretical foundation of DINEOF and proof of its most

523

important property of convergency that makes DINEOF a useful approach to reconstruct an

524

incomplete data matrix.

525

a. Best k -dimension linear model

526

Denote data matrix as \mathbf{A} containing observations. \mathbf{A}_{ij} represents the value of the field

527

$f(r, t)$ at location r_i and moment t_i :

528
$$\mathbf{A}_{ij} = f(r_i, t_j) \tag{B1}$$

529 Define \mathbf{X} as a low-dimension linear matrix that approximates \mathbf{A} . Thus \mathbf{A}_{ij} is equal to \mathbf{X}_{ij}
 530 plus an error.

531
$$\mathbf{A}_{ij} = \mathbf{X}_{ij} + \delta \tag{B2}$$

532 We assume the error is from Gaussian distribution with zero mean and standard deviation
 533 δ , thus $\mathbf{A}_{ij} \sim N(\mathbf{X}_{ij}, \delta)$

534 We regard \mathbf{X}_{ij} as a parameter, thus the log-likelihood of \mathbf{A}_{ij} is

535
$$\log\Pr(\mathbf{A}_{ij}|\mathbf{X}_{ij}) = -\frac{1}{2\delta^2}(\mathbf{A}_{ij} - \mathbf{X}_{ij})^2 + C \tag{B3}$$

536 Maximize $\log P(\mathbf{A}|\mathbf{X})$ is equivalent to minimize $\|\mathbf{A} - \mathbf{X}\|_F^2$, where $\|\cdot\|_F$ is Frobenius
 537 Norm. Let $\mathbf{A} = \mathbf{U}\mathbf{\Sigma}\mathbf{V}$ be the singular value decomposition. Given the Eckart-Young theorem,

538
$$\min_{\text{rank}(\tilde{\mathbf{X}}) \leq k} \|\mathbf{A} - \tilde{\mathbf{X}}\|_F^2 = \|\mathbf{A} - \mathbf{U}_k \mathbf{\Sigma}_k \mathbf{V}_k^T\|_F^2 \tag{B4}$$

539 Where \mathbf{U}_k is the top k left singular vectors, $\mathbf{\Sigma}_k$ is the diagonal matrix with entries of top k
 540 singular values, \mathbf{V}_k is the top k right singular vectors.

541 Thus, the best k -rank approximation to \mathbf{A} is given by $\mathbf{X} = \mathbf{U}_k \mathbf{\Sigma}_k \mathbf{V}_k^T$ when \mathbf{A} is a complete
 542 data matrix.

543 *b. Approximation to incomplete data matrix*

544 Iteration of implementing SVD is the key step in DINEOF operation and is belonging to
 545 an EM procedure, which can prove its properties such as convergence and approximation of
 546 unknown data.

547 Incomplete matrix \mathbf{A} comprises two parts: observed data, \mathbf{A}^o and unobserved data \mathbf{A}^u .

548 The complete log-likelihood is given by

$$549 \quad \log P(\mathbf{A}^o, \mathbf{A}^u | \mathbf{X}) = \sum_{\mathbf{A}_{i,j} \in \mathbf{A}^o} \log P(\mathbf{A}_{ij} | \mathbf{X}) + \sum_{\mathbf{A}_{i,j} \in \mathbf{A}^u} \log P(\mathbf{A}_{ij} | \mathbf{X}) \quad (B5)$$

550 In the t th iteration of E-step, the posterior distribution of \mathbf{A}^u is $q^{(t)}(\mathbf{A}^u) =$
551 $\sum_{\mathbf{A}_{i,j} \in \mathbf{A}^u} P(\mathbf{A}_{ij} | \mathbf{X}^{(t-1)})$.

552 The expectation of complete log-likelihood with respect to \mathbf{A}^u is expressed as:

$$553 \quad E_{q^{(t)}} \left(\sum_{\mathbf{A}_{i,j} \in \mathbf{A}^o} \log P(\mathbf{A}_{ij} | \mathbf{X}^{(t)}) + \sum_{\mathbf{A}_{i,j} \in \mathbf{A}^u} \log P(\mathbf{A}_{ij} | \mathbf{X}^{(t)}) \right)$$

$$554 \quad = \sum_{\mathbf{A}_{i,j} \in \mathbf{A}^o} \log P(\mathbf{A}_{ij} | \mathbf{X}^{(t)}) + E_{q^{(t)}} \left(\sum_{\mathbf{A}_{i,j} \in \mathbf{A}^u} \log P(\mathbf{A}_{ij} | \mathbf{X}^{(t)}) \right) \quad (B6)$$

555 Here,

$$556 \quad \sum_{\mathbf{A}_{i,j} \in \mathbf{A}^o} \log P(\mathbf{A}_{ij} | \mathbf{X}^{(t)}) = -\frac{1}{2\delta^2} (\mathbf{A}_{ij} - \mathbf{X}_{ij}^{(t)})^2 + C \quad (B7)$$

$$557 \quad E_{q^{(t)}} (\log P(\mathbf{A}_{ij} | \mathbf{X}^{(t)}))$$

$$558 \quad = -\frac{1}{2\delta^2} E_{q^{(t)}} \left((\mathbf{A}_{ij} - \mathbf{X}_{ij}^{(t)})^2 \right) + C$$

$$559 \quad = -\frac{1}{2\delta^2} (E_{q^{(t)}}(\mathbf{A}_{ij}^2) - E_{q^{(t)}}(2\mathbf{A}_{ij}\mathbf{X}_{ij}^{(t)}) + E_{q^{(t)}}(\mathbf{X}_{ij}^{(t)})^2) + C$$

$$560 \quad = -\frac{1}{2\delta^2} \left((\mathbf{X}_{ij}^{(t-1)})^2 + \delta^2 - 2\mathbf{X}_{ij}^{(t-1)}\mathbf{X}_{ij}^{(t)} + (\mathbf{X}_{ij}^{(t)})^2 \right) = -\frac{1}{2\delta^2} (\mathbf{X}_{ij}^{(t-1)} - \mathbf{X}_{ij}^{(t)})^2 + C \quad (B8)$$

561 Thus, the expectation of the complete log-likelihoods can be written as

$$562 \quad -\frac{1}{2\delta^2} \left(\sum_{\mathbf{A}_{i,j} \in \mathbf{A}^o} (\mathbf{A}_{ij} - \mathbf{X}_{ij}^{(t)})^2 + \sum_{\mathbf{A}_{i,j} \in \mathbf{A}^u} (\mathbf{X}_{ij}^{(t-1)} - \mathbf{X}_{ij}^{(t)})^2 \right) + C \quad (B9)$$

563

564 Unobserved \mathbf{A}_{ij} is filled with $\mathbf{X}_{ij}^{(t-1)}$ at time t . The maximum expectation is equivalent to

565
$$\operatorname{argmin}_{\mathbf{X}} \sum (\mathbf{A}_{ij} - \mathbf{X}_{ij}^{(t)})^2$$

566 Thus, the optimal value $\mathbf{X}_{ij}^{(t)}$ can be obtained by performing SVD on \mathbf{A}^t .

567 This EM procedure guarantees convergence (Lin 2011).

568

569

REFERENCES

- 570 Alvera-Azcárate, A., A. Barth, M. Rixen, and J. M. Beckers, 2005: Reconstruction of
571 incomplete oceanographic data sets using empirical orthogonal functions: application to the
572 Adriatic Sea surface temperature. *Ocean Modelling*, **9**, 325-346,
573 <https://doi.org/10.1016/j.ocemod.2004.08.001>.
- 574 Alvera-Azcárate, A., A. Barth, J.-M. Beckers, and R. H. Weisberg, 2007: Multivariate
575 reconstruction of missing data in sea surface temperature, chlorophyll, and wind satellite
576 fields. *Journal of Geophysical Research: Oceans*, **112**,
577 <https://doi.org/10.1029/2006JC003660>.
- 578 Alvera-Azcárate, A., A. Barth, G. Parard, and J.-M. Beckers, 2016: Analysis of SMOS sea
579 surface salinity data using DINEOF. *Remote Sensing of Environment*, **180**, 137-145,
580 <https://doi.org/10.1016/j.rse.2016.02.044>.
- 581 Antoine, D., J.-M. André, and A. Morel, 1996: Oceanic primary production: 2. Estimation at
582 global scale from satellite (Coastal Zone Color Scanner) chlorophyll. *Global Biogeochemical*
583 *Cycles*, **10**, 57-69, [10.1029/95GB02832](https://doi.org/10.1029/95GB02832).
- 584 Aumont, O., C. Ethé, A. Tagliabue, L. Bopp, and M. Gehlen, 2015: PISCES-v2: an ocean
585 biogeochemical model for carbon and ecosystem studies. *Geosci. Model Dev.*, **8**, 2465-2513,
586 [10.5194/gmd-8-2465-2015](https://doi.org/10.5194/gmd-8-2465-2015).
- 587 Beckers, J. M., and M. Rixen, 2003: EOF Calculations and Data Filling from Incomplete
588 Oceanographic Datasets. *Journal of Atmospheric and Oceanic Technology*, **20**, 1839-1856,
589 [10.1175/1520-0426\(2003\)020<1839:ECADFF>2.0.CO;2](https://doi.org/10.1175/1520-0426(2003)020<1839:ECADFF>2.0.CO;2).
- 590 Beckers, J. M., A. Barth, and A. Alvera-Azcárate, 2006: DINEOF reconstruction of clouded
591 images including error maps – application to the Sea-Surface Temperature around
592 Corsican Island. *Ocean Sci.*, **2**, 183-199, [10.5194/os-2-183-2006](https://doi.org/10.5194/os-2-183-2006).
- 593 Behrenfeld, M. J., and E. S. Boss, 2014: Resurrecting the Ecological Underpinnings of Ocean
594 Plankton Blooms. *Annual Review of Marine Science*, **6**, 167-194, [10.1146/annurev-marine-052913-021325](https://doi.org/10.1146/annurev-marine-052913-021325).
- 596 Behrenfeld, M. J., and Coauthors, 2006: Climate-driven trends in contemporary ocean
597 productivity. *Nature*, **444**, 752-755, [10.1038/nature05317](https://doi.org/10.1038/nature05317).

- 598 Benedetti, F., M. Vogt, U. H. Elizondo, D. Righetti, N. E. Zimmermann, and N. Gruber,
599 2021: Major restructuring of marine plankton assemblages under global warming. *Nature*
600 *Communications*, **12**, 5226, 10.1038/s41467-021-25385-x.
- 601 Blondeau-Patissier, D., J. F. R. Gower, A. G. Dekker, S. R. Phinn, and V. E. Brando, 2014: A
602 review of ocean color remote sensing methods and statistical techniques for the detection,
603 mapping and analysis of phytoplankton blooms in coastal and open oceans. *Progress in*
604 *Oceanography*, **123**, 123-144, <https://doi.org/10.1016/j.pocean.2013.12.008>.
- 605 Cole, H., S. Henson, A. Martin, and A. Yool, 2012: Mind the gap: The impact of missing data
606 on the calculation of phytoplankton phenology metrics. *Journal of Geophysical Research:*
607 *Oceans*, **117**, 10.1029/2012JC008249.
- 608 Ghahramani, Z., and M. Jordan, 1993: Supervised learning from incomplete data via an EM
609 approach. *Advances in neural information processing systems*, **6**.
- 610 Gobler, C. J., O. M. Doherty, T. K. Hattenrath-Lehmann, A. W. Griffith, Y. Kang, and R. W.
611 Litaker, 2017: Ocean warming since 1982 has expanded the niche of toxic algal blooms in the
612 North Atlantic and North Pacific oceans. *Proceedings of the National Academy of Sciences*,
613 **114**, 4975-4980, 10.1073/pnas.1619575114.
- 614 Hilborn, A., and M. Costa, 2018: Applications of DINEOF to Satellite-Derived Chlorophyll-a
615 from a Productive Coastal Region. *Remote Sensing*.
- 616 Huntington, H. P., and Coauthors, 2020: Evidence suggests potential transformation of the
617 Pacific Arctic ecosystem is underway. *Nature Climate Change*, 10.1038/s41558-020-0695-2.
- 618 Kahru, M., V. Brotas, M. Manzano-Sarabia, and B. G. Mitchell, 2011: Are phytoplankton
619 blooms occurring earlier in the Arctic? *Global Change Biology*, **17**, 1733-1739,
620 10.1111/j.1365-2486.2010.02312.x.
- 621 Keerthi, M. G., C. J. Prend, O. Aumont, and M. Lévy, 2022: Annual variations in
622 phytoplankton biomass driven by small-scale physical processes. *Nature Geoscience*, **15**,
623 1027-1033, 10.1038/s41561-022-01057-3.
- 624 Kurucz, M., A. A. Benczúr, and K. Csalogány, 2007: Methods for large scale SVD with
625 missing values. *Proceedings of KDD cup and workshop*, Citeseer, 31-38.
- 626 Lewis, K. M., G. L. van Dijken, and K. R. Arrigo, 2020: Changes in phytoplankton
627 concentration now drive increased Arctic Ocean primary production. *Science*, **369**, 198,
628 10.1126/science.aay8380.
- 629 Lin, D., 2011: An Introduction to Expectation-Maximization.
- 630 Liu, X., and M. Wang, 2018: Gap Filling of Missing Data for VIIRS Global Ocean Color
631 Products Using the DINEOF Method. *IEEE Transactions on Geoscience and Remote*
632 *Sensing*, **56**, 4464-4476, 10.1109/TGRS.2018.2820423.
- 633 ———, 2019: Filling the Gaps of Missing Data in the Merged VIIRS SNPP/NOAA-20 Ocean
634 Color Product Using the DINEOF Method, **11**, 178.
- 635 Mahadevan, A., 2005: Spatial Heterogeneity and Its Relation to Processes in the Upper
636 Ocean. *Ecosystem Function in Heterogeneous Landscapes*, G. M. Lovett, M. G. Turner, C.
637 G. Jones, and K. C. Weathers, Eds., Springer New York, 165-182.
- 638 Marchese, C., B. P. V. Hunt, F. Giannini, M. Ehrler, and M. Costa, 2022: Bioregionalization
639 of the coastal and open oceans of British Columbia and Southeast Alaska based on Sentinel-
640 3A satellite-derived phytoplankton seasonality. *Frontiers in Marine Science*, **9**.

This Work has been submitted to Journal of Atmospheric and Oceanic Technology.
Copyright in this Work may be transferred without further notice.

- 641 Maritorena, S., O. H. F. d'Andon, A. Mangin, and D. A. Siegel, 2010: Merged satellite ocean
642 color data products using a bio-optical model: Characteristics, benefits and issues. *Remote*
643 *Sensing of Environment*, **114**, 1791-1804, <https://doi.org/10.1016/j.rse.2010.04.002>.
- 644 Sathyendranath, S., and Coauthors, 2019: An Ocean-Colour Time Series for Use in Climate
645 Studies: The Experience of the Ocean-Colour Climate Change Initiative (OC-CCI). *Sensors*,
646 **19**, 4285.
- 647 Sheng, Z., W. Weihong, J. Ford, F. Makedon, and J. Pearlman, 2005: Using singular value
648 decomposition approximation for collaborative masking. *Seventh IEEE International*
649 *Conference on E-Commerce Technology (CEC'05)*, 257-264.
- 650 Smith, K. E., and Coauthors, 2021: Socioeconomic impacts of marine heatwaves: Global
651 issues and opportunities. *Science*, **374**, eabj3593, doi:10.1126/science.abj3593.
- 652 Yang, Z., X. Xia, F.-Y. Teo, S.-P. Lim, and D. Yuan, 2023: An Improved DINEOF
653 Algorithm Based on Optimized Validation Points Selection Method. *Water*, **15**, 392.
- 654 Zhao, H., 2023: Satellite Perspective on Phytoplankton Bloom Phenology and Linkages With
655 Changing Environments in the Northern High-Latitude Oceans. Ph.D., Indiana State
656 University, 178 pp.
- 657 Zhao, H., A. Matsuoka, M. Manizza, and A. Winter, 2022: Recent Changes of Phytoplankton
658 Bloom Phenology in the Northern High-Latitude Oceans (2003–2020). *Journal of*
659 *Geophysical Research: Oceans*, **127**, e2021JC018346,
660 <https://doi.org/10.1029/2021JC018346>.
- 661
- 662
- 663